Inferring the rheology of the crust from the uplift observed above the Altiplano-Puna Magma Body

Nicolò R Sgreva, Anna Massmeyer, Anne Davaille

Inferring the rheology of the crust from the uplift observed above the Altiplano-Puna Magma Body

Nicolò R. Sgreva[a,*], Anna Massmeyer[b], Anne Davaille[c]

[a] *Université de Lorraine, CNRS, LEMTA, 54000, Nancy, France*
[b] *Institute of Heat and Mass Transfer, RWTH Aachen University, Augustinerbach 6, 52056 Aachen, Germany*
[c] *Université Paris-Saclay, CNRS, FAST, 91405, Orsay, France*

Abstract

Geophysical imaging techniques together with numerical models have shown that the surface uplift measured above the Altiplano-Puna Magma Body (APMB) can be resolved by the presence and propagation of a diapir from the top of the APMB itself. In this work we interpret deformations that characterize the crustal region above and around APMB through the employment of a viscoplastic type rheology. That is, we assume that at large scale the ductile lower-middle crust that surround the magmatic mush behaves as yield-stress fluid described by a Herschel-Bulkley (HB) model. In this scenario, the main critical conditions needed for the growth and the subsequent rise of the diapir are: (1) the ratio between yield stress and viscous stresses, namely the Bingham number Bi, has to be less than 1, i.e. $Bi \leq 1$; and (2) the ratio between buoyancy stresses and yield stress, namely the inverse of the Yield number $Y_{inv}=Y^{-1}$, has to be larger than a critical value, i.e. $Y_{inv} > Y_{inv_C}$. By using these critical conditions we infer the bulk

*nicolo.sgreva@univ-lorraine.fr

rheological properties of the heterogeneous lower-middle crust above APMB. We estimate the yield stress of the crust in between 0.5-15 MPa. For a crust that allows the development and the emerge of a 10 to 100 km wide diapir, the coupling of this range of yield stress with the regional uplift velocity measured at the surface allows to estimate a critical strain rate of $\sim 10^{-15}$-10^{-16} s^{-1} and a maximum bulk effective viscosity of the lower-middle crust of η_c=10^{21} Pa s.

Keywords: Rheology: crust and lithosphere, APMB, Diapirism, Yield stress, Viscoplastic

1. Introduction

The Altiplano-Puna Magma Body (APMB) is a mid-crustal magmatic system located at ∼20 km beneath the Altiplano-Puna Volcanic Complex (APVC) in the central Andes, South America. It represents the largest active, continental magma body in Earth's crust (Zandt et al., 2003) and is considered to be directly related to an uplifting region, centered on the western slope of Uturuncu volcano, and its peripheral subsidence zone (Fig. 1) (Fialko and Pearse, 2012). The entire APMB can be represented as a complex transcrustal magmatic structure, that is a large environment volumetrically dominated by crystal mush (Cashman et al., 2017; Pritchard et al., 2018). Given its impact to the region, a good description of its dynamics becomes crucial to understand both its mobility, lifetime, internal structure (e.g. Massol and Jaupart, 2009; Gonnermann and Manga, 2007; Caricchi et al., 2007; Turner and Costa, 2007) and the role that such an enormous ($\sim 5\times10^5$ km^3, Ward et al. (2014)) magmatic structure can play on the deformation of the

overlying crust.

However, to constrain the mush dynamics beneath APVC and the thermo-mechanical response of the surrounding region, a number of geometrical and physical properties of both APMB and lower-middle crust are required. Some of them have been constrained in recent years by using different geophysical investigation methods. For instance, by combining seismic tomography and 3D-model inversion to evaluate the crustal 3D shear-wave velocity field, Ward et al. (2014) displayed a very large ($\sim 5 \times 10^5$ km^3) low seismic velocity (LSV) zone at a depth of 4-25 km beneath the APVC. This region is interpreted as an hotter zone compared to the surrounding material, and may also be enriched in melt content. A similar broad LSV zone centered below the Uturuncu volcano and at ~15 km below sea level has been revealed also by other authors (e.g. Zandt et al., 2003; Chmielowski et al., 1999). However, due to the resolution of seismic tomography that is not better than 1 km (Cashman et al., 2017), the exact geometry and position of this hot body are still debated. This is caused by the difficulty in constraining the spacial melt distribution with the technique, which is not always able to recognize large melt bodies even in regions that are active nowadays or have produced large eruptions in the Quaternary (Cashman et al., 2017).

Besides seismic tomography, other geophysical imaging techniques can help to better characterize this anomalous structure. Magnetotelluric data reveals a first large low electrical resistivity (<3 Ωm) anomaly at ~15 km below the sea level and a second ~10-km-wide vertical anomaly on the top of it (Fig. 1c) (Comeau et al., 2015, 2016). Differences in resistivity between the two regions may be related to variations in the composition: while the

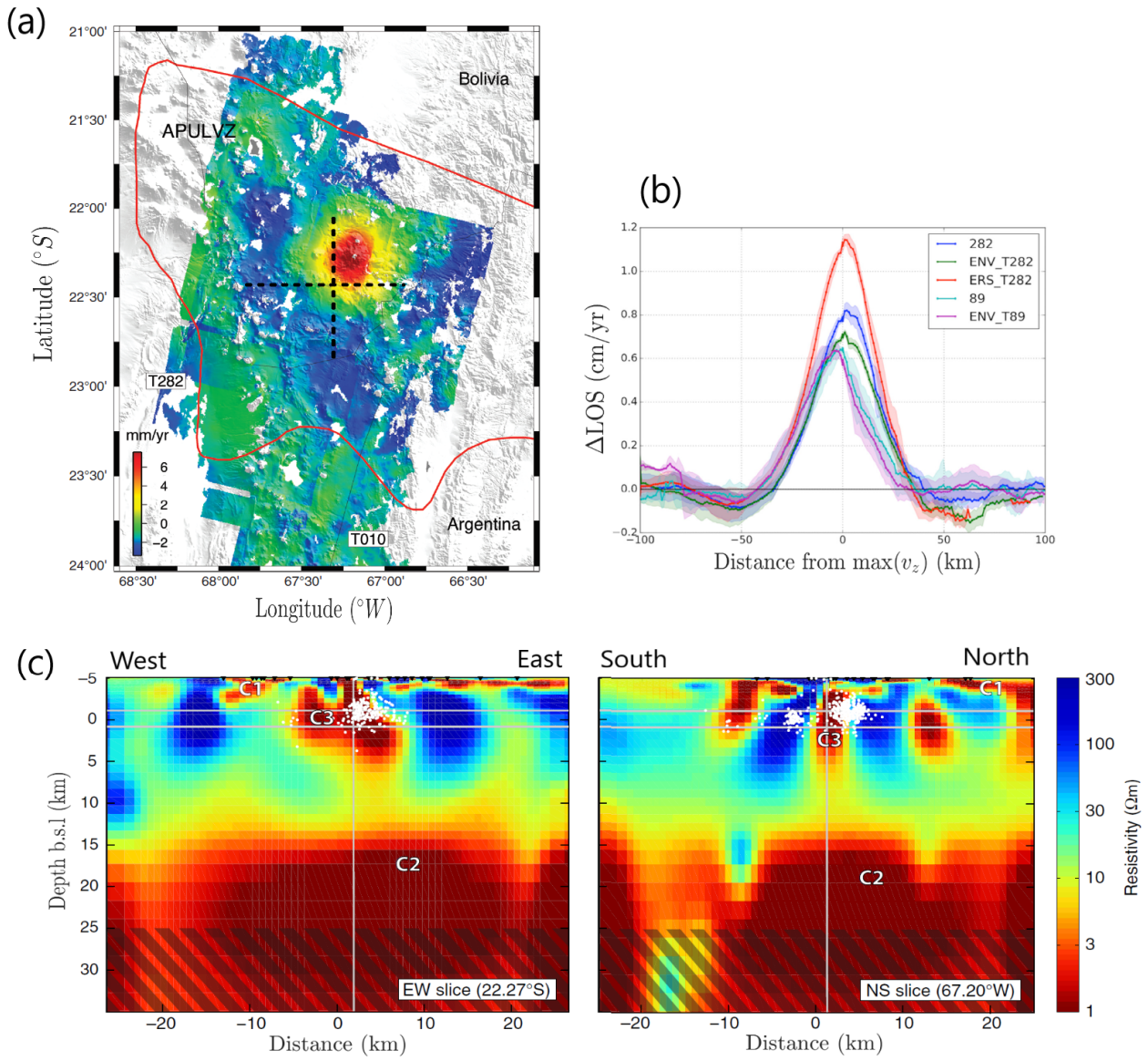

Figure 1: (a) Map view of the Altiplano-Puna region (Southern Bolivia). Colors indicate the elevation rate measured at the surface from InSAR data. Red line indicates the mid-crustal low-velocity zone associated to the APMB. Black dotted lines indicate the locations of cross sections in (c). Modified from Fialko and Pearse (2012). (b) Average velocities of line of sight (LOS) along sections crossing the center of the uplift. Modified from Gottsmann et al. (2017). (c) West-East and South-North vertical cross sections of the 3D resistivity model of (Comeau et al., 2015) across APVC. The main low electrical resistivity anomaly (C2) is associated to the APMB whereas the smaller anomaly on the top of it (C3) is interpreted as an ascent diapir. Modified from Comeau et al. (2016).

resistivity of the first deeper body ("C2" in Fig. 1c) can be explained by the presence of andesite melts in APMB (with a melt fraction ϕ_f >0.15), the resistivity of the region above it ("C3" in Fig. 1c) may reflect the presence of dacite melts combined with aqueous fluids (Comeau et al., 2016). A similar vertically elongated structure is revealed also by the inversion of Bouguer anomaly data that highlights a low density and ∼15-km-wide structure on the top of the APMB (del Potro et al., 2013), interpreted as an active diapiric ascent of magma (e.g. del Potro et al., 2013; Fialko and Pearse, 2012; Gottsmann et al., 2017). The presence of a mid-crustal diapir which slowly moves upward is in agreement with geodesy data collected above APMB from 1995 to 2010 (Fialko and Pearse, 2012). InSAR data show indeed a ∼150-km-wide region, centered on the western slope of Uturuncu volcano, which is uplifted at the rate of ∼1 cm/yr, and surrounded by an approximately 30-km-wide ring of subsidence (Fig. 1a-b). The morphology and large extent of such a "sombrero"-shaped deformation on the surface cannot be caused by a single large dike as expected for an intrusion in a merely elastic crust (Menand and Tait, 2001; Jellinek and DePaolo, 2003). But instead it matches well results of geodynamics models that assume the rise of a large diapir fed by partial melt from the APMB within a crust that is not-purely elastic (e.g. Fialko and Pearse, 2012; Gottsmann et al., 2017). Such a large diapir rising from the top of APMB would cause an extensive deformation of the whole crust, leading in turn to the displacement measured at the surface by geodesy techniques.

The interaction of the rising diapir with the crustal layer above offers the opportunity to estimate the effective rheology of the crust itself. The structure of the crust with its rheological properties and mechanical behavior

are indeed heavily influenced by the specific geodynamic context in which the crust is located (Burov, 2011). So the rheology can in fact deviate from the classical case where the whole deformation can be simply described by a purely elastic or a purely viscous model. Moreover, heterogeneities that characterize the crust on all scales, i.e. from small-scale (e.g. grain size, pore fluid pressure, chemical activities of mineral components, etc.) to large-scale (dikes filled with magma, faults, etc.), result in an intricate structure that can easily be locked or "jammed". Thus at the macroscopic scale, the crust bulk behavior could be comparable to that of a yield-stress material whereby flow can only occur when a threshold stress value (i.e. the yield stress, σ_y) is reached (Ancey, 2007; Bonn et al., 2017). Within this perspective, for an heterogeneous lower-middle crust an effective viscoplastic rheology can be claimed, making the yield stress a key aspect to better understand its bulk behavior.

In this paper we infer the rheological properties of the lower-middle crust below APVC from the rate of vertical surface displacement measured in the orogenic region of the Altiplano and by assuming that this uplift is caused by the rise of a diapir from above APMB. To do so we assume that the heterogeneous crust surrounding the diapir behaves as a non-Newtonian yield stress fluid, i.e. as a material whose bulk behavior can be described with a viscoplastic rheological model. In section 2 we introduce the main rheological properties of these materials. In section 3 we discuss the general critical conditions for motion of a buoyant body through an yield stress fluid. The latter are applied to the APMB case in section 4. We end by discussing the implications that our results have for a partially molten lower-middle crust.

2. The yield-stress in viscoplastic rheology

Viscoplastic fluids (synonym of yield stress fluids) are characterized by the presence of a yield stress, σ_y (Dinkgreve et al., 2017). A typical example of them is a suspension of particles in a liquid. When the particle volume fraction increases, the particles come into close contact, and the material can face jamming. In this jammed state, the material can support stresses without flowing. A so-called yield stress fluid does not flow unless the applied stresses are large enough to unjam the structure, but it does flow when the stresses become larger than σ_y. This introduces a non-linearity to the material rheology, with strong impact on its dynamics (Makse et al., 2005; Coussot, 2005; Barnes, 1995).

Simple yield stress fluids are those described by popular rheological models such as the Bingham model or the Hershel-Bulkley (HB) model. The latter writes

$$\begin{aligned} \sigma = \sigma_y + K_v \dot{\gamma}^n \qquad & \text{for} \qquad \sigma > \sigma_y \\ \dot{\gamma} = 0 \qquad & \text{for} \qquad \sigma \leq \sigma_y \end{aligned} \tag{1}$$

where σ is the stress, $\dot{\gamma}$ the strain rate, K_v the consistency and n the power-law exponent. Note that the exponent n defined here is the reverse of the power law index usually used in equations for creep mechanisms in geophysics (e.g. in Ranalli, 1995). For n <1 the fluid is shear thinning and the effective viscosity $\eta_{eff} = \sigma/\dot{\gamma}$ decreases as $\dot{\gamma}$ increases. For n >1 the fluid is shear thickening. For n=1 and $\sigma_y > 0$ the HB model reduces to the

Bingham model and describes a fluid with a linear flow curve and constant value of viscosity. And, finally, for n=1 and σ_y=0 the fluid is Newtonian.

The concepts of yield stress and plasticity are not only employed in the rheology of viscoplastic fluids, but they are also largely used in solid mechanics through the Coulomb plasticity theory. In Coulomb plasticity, plastic deformation indicates the irreversible deformation of a sample under stress whereas in Bingham viscoplasticity it refers to a solid-liquid transition. In this latter case the yield stress becomes the limit between the elastic (or viscoelastic) solid-like domain and the viscous fluid-like domain where the material flows. Even though the definition of σ_y is not the same among the two theories, the concept behind it relies to some overlapping phenomena: the transition from a reversible to a non-reversible deformation on one side and the not-flowing to flowing on the other side. Besides that, however, the two theories show some differences on their theoretical formulation (Ancey, 2007). The main one regards the description of material's deformation on a macroscopic scale: a viscoplastic fluid behaves as a whole on the bulk scale, i.e. as a one-phase homogeneous material (Coussot et al., 2009). Hence, it only requires a single stress-strain constitutive equation, e.g. eq.(1), where there is no need to separate the role of interstitial fluids from the one of the solid phase. This strongly differs from a two-phases saturated Coulomb material in which the two phases can move at different velocities and have to be considered separately.

Throughout the rest of this article, we will always refer for the fluid deformation to the rheological viscoplastic description. That is describing both mush and hot crust as a single-phase incompressible fluid that behaves

as a viscous fluid once set in motion.

3. Conditions for the ascent of a buoyant instability in a yield-stress fluid

When a yield stress fluid is heated the buoyancy stresses that originate due to thermal expansion may not be large enough to exceed the fluid yield stress. Motion is then prevented and the fluid remains at rest. On the other hand, when local stresses are large enough, a thermal plume can develop and rise within the fluid column. The plume dynamics has been investigated experimentally for a simple yield stress fluid heated by a local heat source by Davaille et al. (2013) (see Appendix A for details on experimental conditions). They found that the formation and subsequent growth of a thermal instability can be described in three main stages: (1) a no-motion phase where a hot pocket grows by thermal diffusion around the localized heat source (Fig. 2a and Fig. 3). (2) A stage where slow creep takes place within the growing hot pocket (Fig. 2b). This slow ascent can be observed also in the spatio-temporal evolution shown in Fig. 3 where bright lines that correspond to reflecting particles formed by Thermo-Liquid Crystals (TLCs) are not longer horizontal but begin to move upward. This is because, starting from this stage, the edge of the thermal pocket begins to empty slowly to feed a creep confined around the heating element (Fig. 2c). However, during this phase the fluid outside the hot pocket still remains unyielded. And (3) the stage in which a hot finger rises upward (Fig. 4a). Here upwelling occurs only within the thermal anomaly and shear is strongly localized along plume boundaries (Fig. 4b). The fluid within the anomaly moves then as a

plug and the overall thermal shape looks more like a finger than the classical mushroom shape expected for Newtonian fluids.

For small Reynolds numbers, the flow resulting from the rising of the thermal instability can be parameterized by two key dimensionless numbers. The first is the Yield number, Y, and the second is the Bingham number, Bi (Davaille et al., 2013; Karimfazli et al., 2016; Massmeyer et al., 2013). For simplicity here we use the inverse of the Yield number, $Y_{inv} = 1/Y$, which represents the ratio between the buoyancy stress and the yield stress. It is usually written as

$$Y_{inv} = \frac{g\Delta\rho\, D}{3\sigma_y}. \tag{2}$$

where g is the acceleration due to gravity and $\Delta\rho$ the density difference between the hot body, described by a characteristic diameter D, and the ambient fluid. Y_{inv} has been firstly employed to evaluate motion of a single rigid sphere in Bingham fluid (Beris et al., 1985). In this case, the critical value of the (inverse) Yield number, Y_{inv_C}, below which the sphere does not move is Y_{inv_C}=6.99. It has been subsequently confirmed experimentally for simple HB fluids (Tabuteau et al., 2007) and for more heterogeneous HB fluids (Sgreva et al., 2020a). In the case of buoyant thermal instabilities instead of spheres, one can consider the hot pocket forming around the heating source at stage (1) and (2) as a buoyant "entity" that tries to go up because it is less dense but is kept anchored at the original position by the fluid yield stress. Davaille et al. (2013) found that the thermal instability will rise only if $Y_{inv} > Y_{inv_C} = 8.8 \pm 0.7$, a value close to but different from the solid sphere case. This is expected given the different geometries and

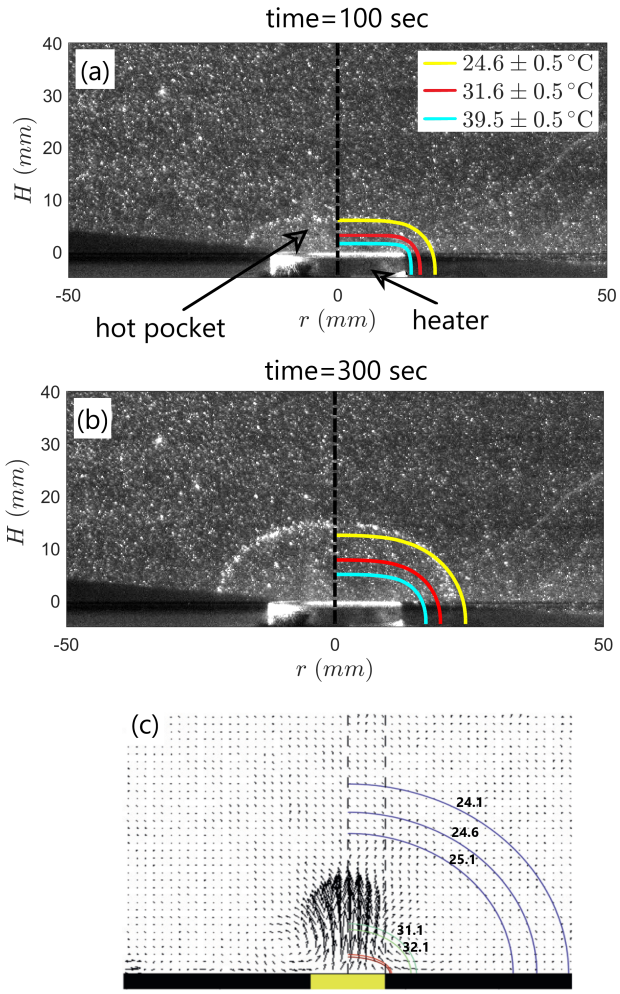

Figure 2: Front view of the growth of a hot pocket in a simple Herschel-Bulkley (HB) fluid (Carbopol) when heated from a localized heating source. Experiment from Davaille et al. (2013), see Appendix A for details on experimental conditions. In (a) and (b) the brighter lines are thermochromic liquid crystals' isotherms. The same isotherms are reproduced numerically in the conductive regime and plotted with different colors: yellow (24.6±0.5 °C), red (31.6±0.5 °C) and blue (39.5±0.5 °C). Time is measured from the start of heating. (a) Growth of a hot pocket. Numerical isotherms fit well the experimental ones (stage (1) in the text). (b) Slow creep stage where the difference between experimental and numerical isotherms indicates the departure from the fully conductive regime (stage (2)). (c) Example of velocity field obtained during the slow creep stage. Solid lines indicate analytical isotherms for a steady-state conductive regime (values are indicated in °C). Significant vertical velocities are recorded at the center of the hot pocket and near the heater while outside the hot pocket the fluid remains motionless.

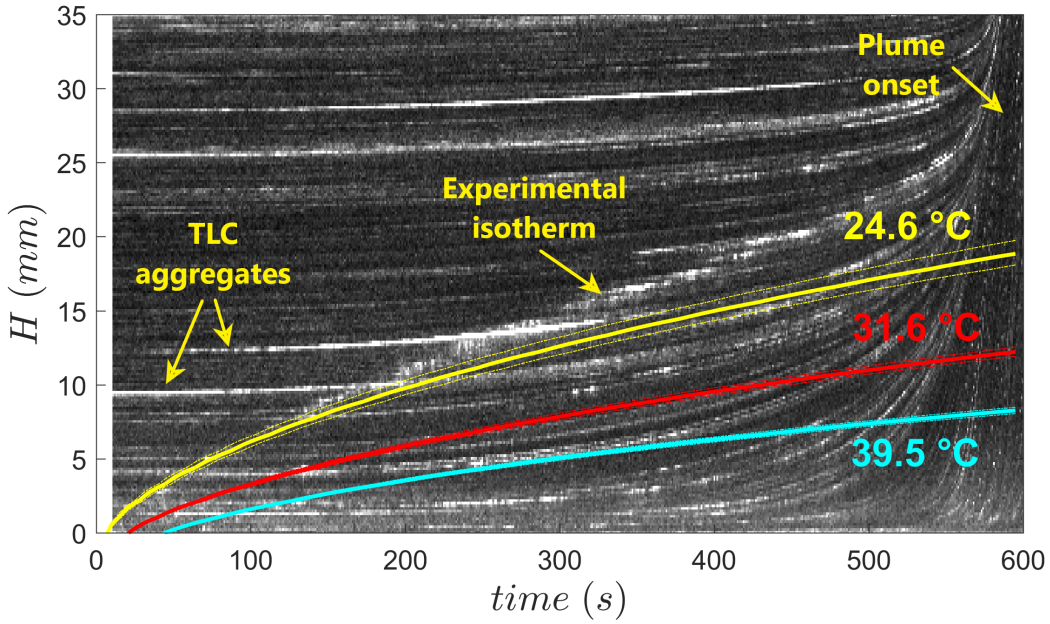

Figure 3: Spatiotemporal evolution of the experiment shown in Fig. 2. The figure shows the light intensity of the pixel line in the center of the setup as a function of time. Colored lines refer to the computed isotherms described in Fig. 2.

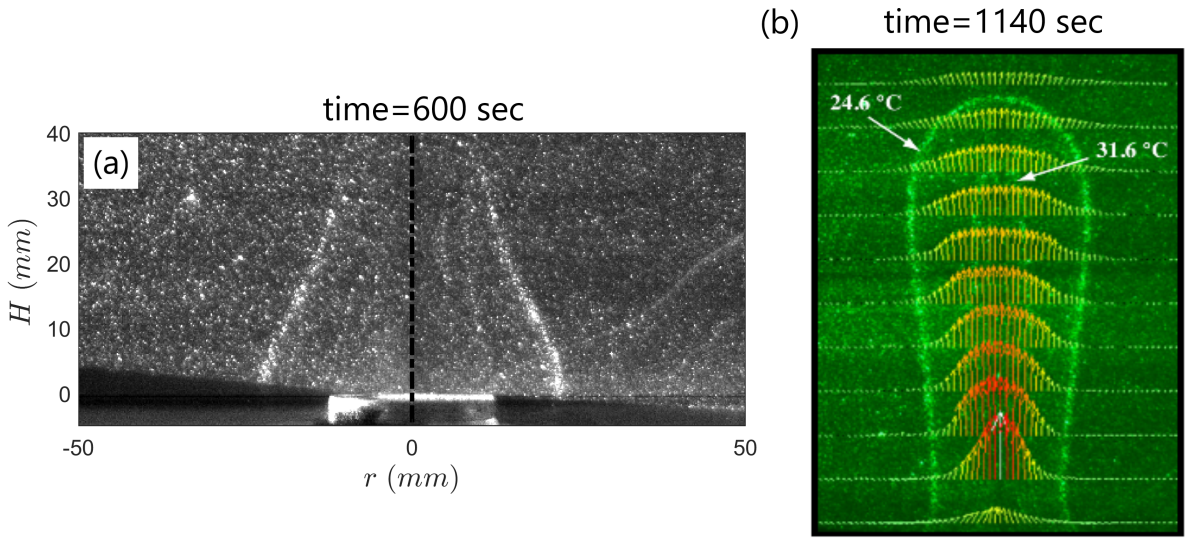

Figure 4: Last stage of the experiment shown in Fig. 2. (a) Rising of the hot plume, corresponding to stage (3) in the text. (b) Developed plume. Bright lines are isotherms. Colored vectors show the velocity field. Adapted from Davaille et al. (2013).

boundaries conditions, i.e. a bottom rigid boundary condition and a fluid-fluid interface between hot pocket and ambient fluid in plume experiments, and a bottom free surface boundary condition and a solid-fluid interface in the experiments for the falling sphere. Y_{inv_C} has been afterwards evaluated also from numerical simulations which investigate the development of thermal plumes in a locally heated simple yield stress fluid (Massmeyer et al., 2013; Sgreva, 2020b). For conditions similar to the experiments of Davaille et al. (2013), namely a comparable fluid rheology, geometry of the setup and imposed heating rate, they led to $Y_{inv_C} = 5.0 \pm 1.2$ in Massmeyer et al. (2013) and 7.35 ± 0.35 in Sgreva (2020b) (Fig. 5). Differences in this case can be related to the formulation of the numerical model, i.e. whether elastic deformation in addition to viscoplasticity is used (Sgreva, 2020b) or not (Massmeyer et al., 2013).

For a more geological perspective, the Yield number has already been used, for instance, to describe the difficulties for magma transport in a dyke through fracturing lithospheric rocks due to buoyancy forces (Weinberg and Podladchikov, 1994). Although the formulation of Y_{inv} in this last case remains the same as ours, by the definition of yield stress, Y_{inv} can evaluate a different physical phenomena. For example, in Weinberg and Podladchikov (1994) the yield stress used to calculate the Yield number is the rock's brittle strength defined following Byerlee's law. The result for transporting magma through dikes is that the condition of $Y_{inv} > Y_{inv_C}$ is very difficult to achieve and to maintain without invoking other quite specific conditions, i.e. very large magma bodies, proximity to the surface, tensile tectonics, etc.

Beside Y, diapir development also requires the Bingham number, Bi,

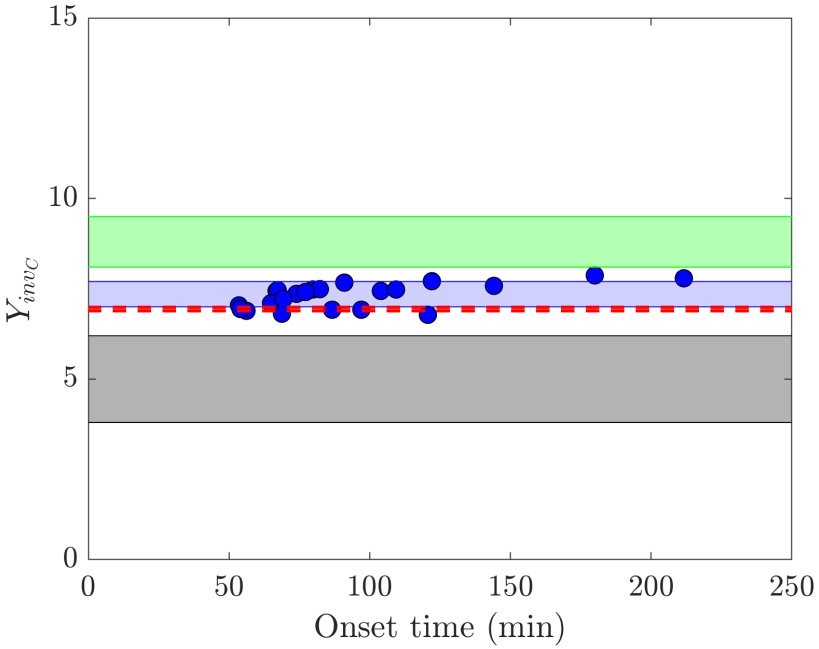

Figure 5: Inverse of the Yield number at the onset (Y_{inv_C}). Blue dots are simulations from Sgreva (2020b) and the blue bar corresponds to Y_{inv_C}=7.35 ± 0.35. Green bar indicates Y_{inv_C}=8.8 ± 0.7 (Davaille et al., 2013), gray bar Y_{inv_C}=5.0 ± 1.2 (Massmeyer et al., 2013) and red dashed line Y_{inv_C}=6.99 (Beris et al., 1985; Tabuteau et al., 2007).

being supercritical, i.e. $Bi \leq 1$ (Massmeyer et al., 2013). The Bingham number compares the yield stress to the viscous stress and for a Herschel-Bulkley fluid writes:

$$Bi = \frac{\sigma_y}{K_v \dot{\gamma}^n}. \tag{3}$$

Motion is therefore expected only when local shear rates are larger than the critical strain rate corresponding to Bi=1, that is for $\dot{\gamma} > \dot{\gamma}_c = (\sigma_y / K_v)^{1/n}$ (Fig. 6). It is only when the shear rate reaches this threshold that the hot pocket that grows from the hypothetical heating point evolves into a diapir. Note that when $Bi = 1$, the stress defined in eq. (1) is $\sigma_c = \sigma_y + K_v \dot{\gamma}_c^n = 2\sigma_y$ and the effective critical viscosity writes:

$$\eta_c = \frac{\sigma_c}{\dot{\gamma}_c} = \frac{2\sigma_y}{(\sigma_y / K_v)^{1/n}}. \tag{4}$$

After the onset, the Bingham number decreases toward a value smaller than one (i.e. $Bi < 1$). For instance, in Sgreva (2020b) and Massmeyer et al. (2013) Bi was found to decrease up to 3 times from the value at the onset when the vertical velocity reaches its maximum (Fig. 6c). This decrease of Bi and the related increase in strain rate (i.e. $\dot{\gamma}/\dot{\gamma}_c > 1$) translates also into smaller effective viscosity. Hence the effective viscosity inferred at the onset ($\eta_{eff} = \eta_c$) represents the largest value of viscosity at which the transition from jamming to motion takes place and it will then decrease ($\eta_{eff} < \eta_c$) during the ascent of the diapir.

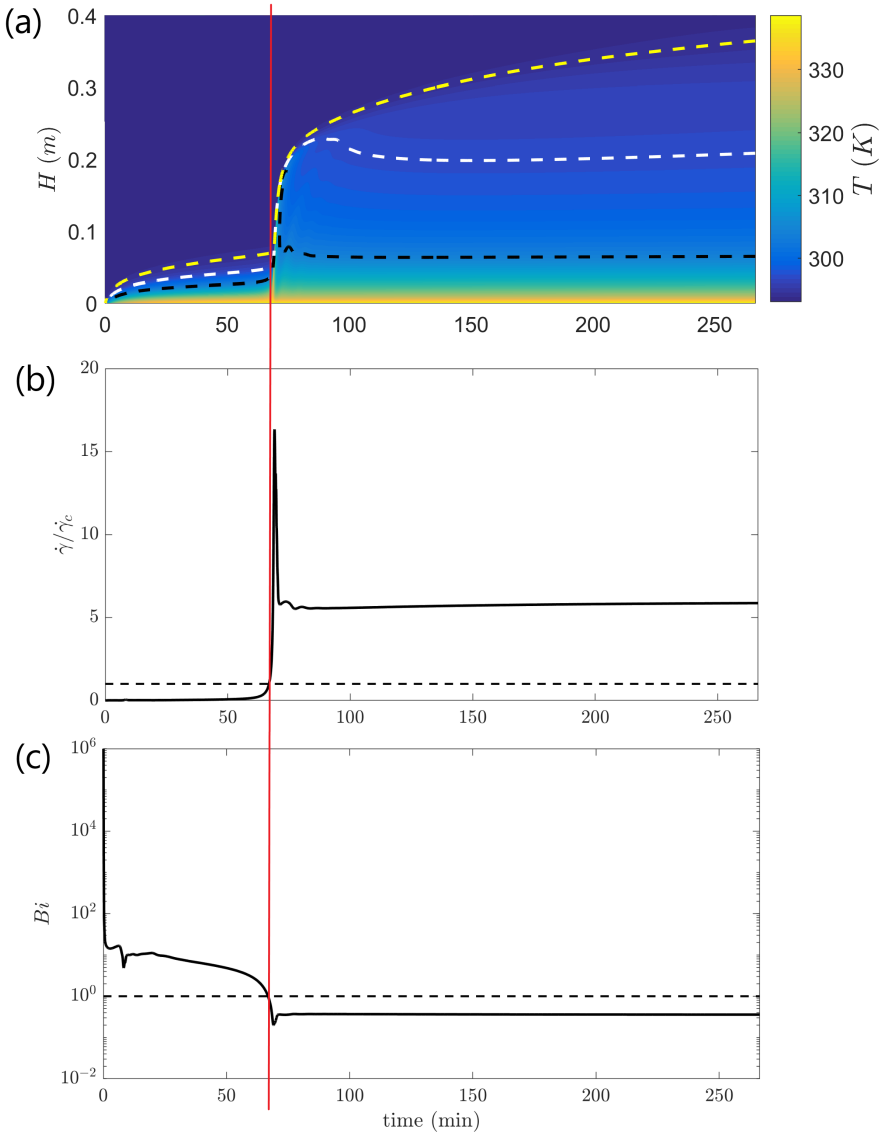

Figure 6: Development of a plume in a HB fluid, from simulation of Sgreva (2020b) ($\Delta T = 44\,^{\circ}$C; $\sigma_y = 0.076$ Pa; $Y_{invC} = 7.44$; $Ra \sim 10^5$). (a) Temporal evolution of temperature T along the central axis. Three isotherms have been highlighted: 21.0 °C (in yellow), 23.9 °C (in white) and 31.1 °C (in black). (b) Evolution of the strain rate $\dot{\gamma}$ normalized by the critical strain rate $\dot{\gamma}_c$ during the development and the rise of the hot instability. The critical strain rate is defined for $Bi = \sigma_y/(K_v\dot{\gamma}_c^n) = 1$. Dashed line indicated $\dot{\gamma}/\dot{\gamma}_c$=1. (c) Evolution of Bingham number. Dashed line indicated Bi=1. The vertical red line indicates when the Bingham number in (c) becomes one.

4. Constraints on the diapirism at APMB and crust's rheology

An active and rising diapir has been suggested as the cause of the uplift observed above the Altiplano-Puna Magma Body (Fialko and Pearse, 2012; Comeau et al., 2015). Geodesy data and leveling data show in fact a continuous (since 1960s), nearly constant and slow uplifting of an about 100-km-wide region of the Altiplano-Puna volcanic complex (Fialko and Pearse, 2012; Henderson and Pritchard, 2013; del Potro et al., 2013). The central area which is being uplifted at about 1 cm/yr is also surrounded by a broad ring of subsidence forming a global sombrero-shape uplift which is consistent with the presence of a diapir deep inside the crust. In this case the diapir would develop from the APMB within a framework of a heterogeneous crust and at greater depth than the brittle-ductile transition. The latter is reported between 4.5 and 10 km below the Altiplano (Jay et al., 2012) whereas the APMB extends from a depth of $\sim$20 km below the surface (Comeau et al., 2015).

In the previous section we have shown how that two main conditions must be satisfied to allow the ascent of a buoyant instability in a yield stress medium. The first one regards the inverse of the Yield number (here we consider $Y_{inv} > Y_{inv_C}= 7.35 \pm 0.35$ from Sgreva (2020b)), while the second one is accounted by $Bi \leq 1$. Given these two conditions, one can evaluate the emplacement conditions for a buoyant instability (e.g. a diapir) in a jammed crustal mush with HB rheology. We do so for the case of APMB, assuming that the uplift measured at the surface originates from the rising of a hot diapir from the shallowest regions of the magmatic reservoir beneath Ulturuncu volcano and rises with a vertical velocity equal to what is measured

at the surface, i.e. v_z=1 cm/yr (Fialko and Pearse, 2012).

In Fig. 7, we show conditions which lead to $Y_{inv} = Y_{inv_C}$ for such a system. According to geodesy data (Fialko and Pearse, 2012; Gottsmann et al., 2017) and magnetotellurics (Comeau et al., 2016), we assume a characteristic diameter D_{diap}=10−100 km for the diapir. The density contrast between diapir and surrounding crust is not well constrained and varies between different models. Fialko and Pearse (2012) use in their numerical simulations a density difference of $\Delta\rho$=400 kg/m^3, whereas smaller values of ∼100 kg/m^3 are employed for example by Gottsmann et al. (2017) and Spang et al. (2019). A similar range of possible $\Delta\rho$, based on the inversion of gravity anomalies, is given by del Potro et al. (2013). An upper limit for the density contrast of 400 kg/m^3 represents an enormous density anomaly produced by the melting of a large enough amount of material below the observed diapiric body. Given a crust density of ρ_c=2700 kg/m^3, this scenario would require, for instance, the presence of a very large melt fraction (ϕ_f), that is ϕ_f ∼0.9 for a dacitic melt with ρ_d=2300 kg/m^3 (del Potro et al., 2013). On the other hand, an overall smaller density contrast reflects a smaller melt fraction which can decrease towards the limit of $\Delta\rho$=50 kg/m^3 for a fully crystallized dacite (ϕ_f=0; ρ_d=2650 kg/m^3).

Within these ranges of diapir's size and density contrast, we find that a diapir can rise and deform the surrounding crust if the latter has a yield stress within a range of 0.5 and 15 MPa (Fig. 7). Larger values of yield stress clearly need either a broader instability or an unlikely larger density contrast. Here the yield stress has to be interpreted within the rheological definition, i.e. as the stress value needed to unjam a locked medium and to

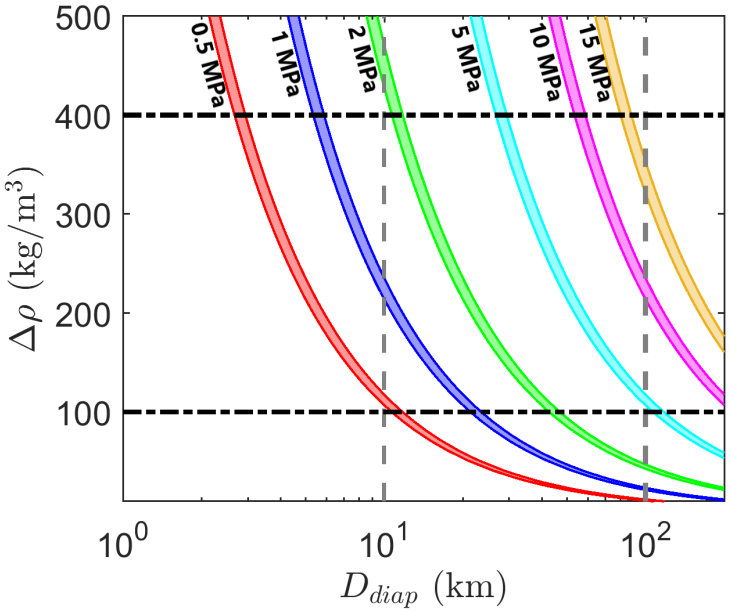

Figure 7: Yield stress (colored lines) allowing the development of a diapir from the top of the APMB according to Y_{inv_C}= 7.35 $\pm$ 0.35, as function of diapir diameter and density contrast.

allow it to flow, rather than the threshold at which the medium simply loses the reversibility in deformation.

Beside $Y_{inv} > Y_{inv_C}$, the other condition for motion is $Bi \leq 1$. As summarized above, this critical condition translates into a critical minimum strain rate required for motion $\dot{\gamma}_c = (\sigma_y/K_v)^{(1/n)}$ and an effective viscosity is then given by $\eta_c = 2\sigma_y/\dot{\gamma}_c$ (eq. (4)). In Fig. 8 we display this viscosity as a function of fluid consistency and the range of yield stress found previously (i.e. σ_y in between 0.5 and 15 MPa). We take two limit values for the shear thinning index, namely n=0.25 (Fig. 8a) and n=0.5 (Fig. 8b). They correspond to stress exponents n_E=1/n in stress-strain relationships for creep of 4 and 2, respectively, as expected for rocks Ranalli (1995). The viscosity reported in Fig. 8 corresponds to the maximum effective viscosity calculated from the minimum strain rate that guarantees Bi=1. As expected from its definition, it depends on the value of fluid consistency that one uses in the HB model. A way to bound the consistency is by taking into account the maximum vertical velocity, v_{max}, at which the thermal instability is moving upward. From the condition $Bi \leq 1$, one can in fact relate v_{max} to the size of the instability and the critical strain rate:

$$v_{max} = C 2 r_{eq} \dot{\gamma}_c, \tag{5}$$

where C is an experimental constant. Based on numerical simulations (Sgreva, 2020b), the maximum velocity is found to scale as $v_{max} \sim 4.45(2r_{eq}\dot{\gamma}_c)$ for constant n=0.58 (Fig. 9). The simulations of Massmeyer et al. (2013) where n was varied between 0.50 and 0.90 present the same trend (Fig. 9). The small differences between the two studies for same n displayed in Fig. 9 can be

related to the different formulation of the numerical model used to simulate plume's formation, namely a regularized viscoplastic model in Massmeyer et al. (2013) and an elasto-viscoplastic model in Sgreva (2020b).

Considering the recorded uplift velocity at the surface v_z as a possible maximum rising velocity of the diapir, for the case at APMB the scaling of v_{max} translates to

$$v_z \sim 4.45 D_{diap} \dot{\gamma}_c, \tag{6}$$

leading to a critical strain rate of $\dot{\gamma}_c = v_z/(4.45 D_{diap})$. Within the chosen interval of D_{diap}, the critical strain rate is $\sim 10^{-15}$-10^{-16} s^{-1}. The resulting consistency is therefore

$$K_v = \sigma_y \dot{\gamma}_c^{-n} = \sigma_y \left(\frac{4.45 D_{diap}}{v_z} \right)^n. \tag{7}$$

This value of K_v is reported in Fig. 8 for the interval of diapir's sizes of 10-100 km.

5. Discussion

Given the evidence of partial melt and the shallow ductile-brittle transition, a simple elastic model for the lower-middle crust beneath APVC is not appropriate to properly describe the whole system but instead a more complicated rheological model is required. The HB framework developed in the previous sections provides estimates of the lower-middle crust effective yield stress and viscosity at APMB.

The first crucial aspect regards the proper definition of yield stress needed to evaluate the conditions of motion. Differently from the already mentioned

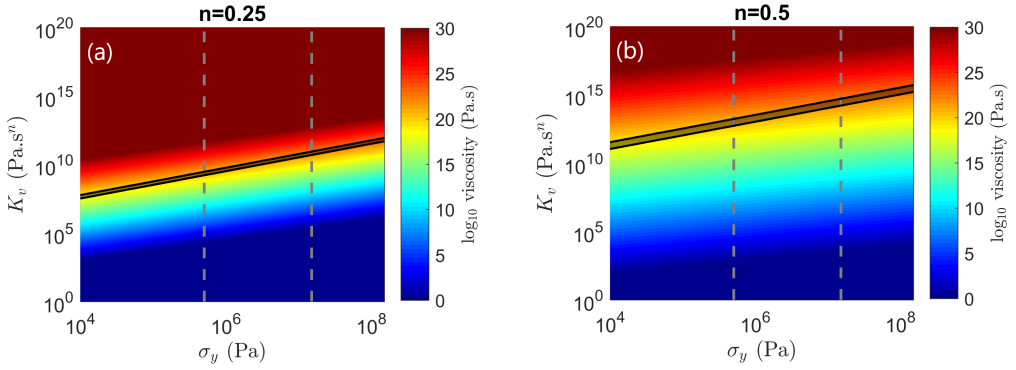

Figure 8: Maximum value of critical effective viscosity η_c (eq.4) corresponding to Bi=1, as function of consistency K_v and yield stress σ_y. Grey dashed lines bound the range of yield stress after Fig. 7. Black bands indicate $K_v = \sigma_y(4.45\, D_{diap}/v_z)^n$, with D_{diap} between 10 and 100 km and an uplift velocity of v_z=1 cm/yr (Fialko and Pearse, 2012). (a) Shear thinning exponent n=0.25 and (b) n=0.5.

work of Weinberg and Podladchikov (1994), in our equation of the Yield number, σ_y does not indicate the stress threshold needed to the brittle failure of the rocks in the crust but it instead represents the threshold to unjam the locked medium, which could for example involve reactivation of fractures and creep. When Y_{inv} is defined to evaluate the ability of the system to transport magma by opening new fractures it must involve yield strength for ambient rocks in the order of 10^2-10^3 MPa, making it dramatically difficult to achieve conditions of $Y_{inv} > Y_{inv_C}$. However, the rheological (jamming) transition in partially molten rocks that takes place when the solid-particles volume fraction (ϕ_s) decreases approaching the maximum packing fraction ($\phi_m \sim$0.6) can lead to a strength drop which can span up to four orders of magnitude (Rosenberg and Handy, 2005; Cashman et al., 2017). In addition to this strong dependence on ϕ_s and hence on the melt fraction ϕ_f, the measurement

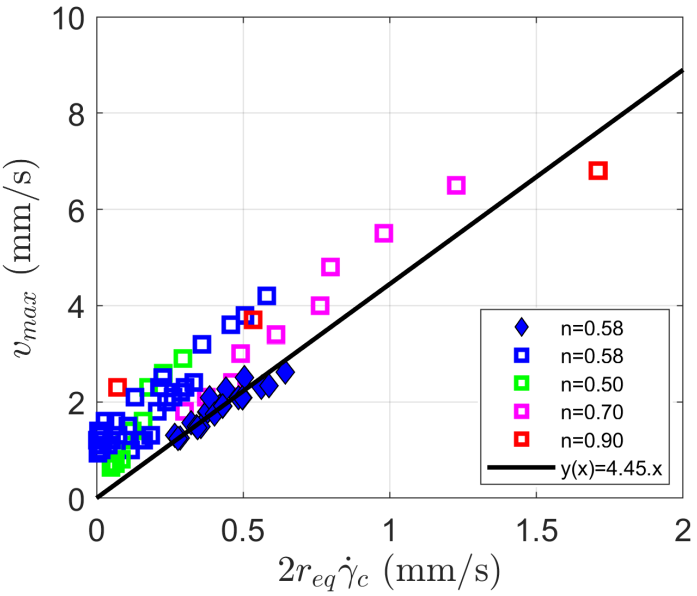

Figure 9: Maximum rising velocity of an hot instability as a function of the product between equivalent diameter $D_{eq} = 2\,r_{eq}$ and critical strain rate. Diamond symbols refer to numerical simulations of thermal plumes in a yield stress fluid of Sgreva (2020b) computed with a power-law index $n = 0.58$. The later are fitted by the equation $y(x) = 4.45\,x$. Squared symbols refer to simulations of Massmeyer et al. (2013) and colors are for the different power-index n tested.

of the strength of a partially molten rock with relative large melt fraction ($\geq$0.3) falls also very close to the minimum measurable value of σ_y from experimental apparatus. The latter is estimated around $\sim$1 MPa (Pistone et al., 2012; Rosenberg and Handy, 2005; Caricchi et al., 2007). In this regard, the range of σ_y of 0.5-15 MPa we found in Fig. 7 for the hot ductile crust that surrounds the rising diapir corresponds, in order of magnitude, to the strength of partially molten granite with ϕ_f $\sim$0.25 in Rosenberg and Handy (2005) (where σ_y $\sim$1 MPa) and those for crustal granitic rocks on the western Arabian Peninsula, where σ_y $\sim$1-3 MPa (Jónsson, 2012).

The second aspect that arises from the ascent of a diapir at APMB regards the values of effective viscosity and strain rate we have found. According to Fig. 7, a diapir of D_{diap}=50 km and $\Delta\rho$=100 kg/m^3 would set on motion and would travel through a crust with yield stress of around σ_y=2.2 MPa. By taking the typical stress exponent expected for creep mechanisms of lower-middle crustal rocks, that is n_E=n^{-1}=3.0 (Ranalli, 1997), the previous conditions lead to a consistency of $\sim$ 10^{13} Pa s$^{0.3}$ and to an effective maximum value of viscosity for the lower-middle crust above APMB of η_c $\sim$ 10^{21} Pa s. This value corresponds to what is needed to trigger the rise of the diapir since it is calculated from the critical condition of Bi=1. However, after the plume onset, Bi continues to decrease (Fig. 6c) while the strain rate increases (Fig. 6b), leading in turn to values of effective viscosity that are lower than those found for Bi=1. From eq. (6), considering a vertical velocity of 1 cm/yr, the critical strain rate results in $\dot{\gamma}_c$ $\sim$$10^{-15}$ s^{-1} for a 50-km-wide diapir. Hence, at conditions of Bi <1 where the strain rate can increase up to one order of magnitude compared with $\dot{\gamma}_c$ (Fig. 6b), we can expect a crustal region that

deforms at a strain rate of 10^{-14} s^{-1}. This corresponds to values of strain rate previously employed for APVC, e.g. $\sim 10^{-14}$ s^{-1} in Jay et al. (2012), and other compression areas, such as Southern-Tibet where $\dot{\gamma} \sim 10^{-14}$-$10^{-15}$ s^{-1} (Wang et al., 2019; Molnar, 2020) and Southern-Aegean where $\dot{\gamma} \sim 10^{-15}$ s^{-1} (Kreemer and Chamot-Rooke, 2004; Kumar and Gordon, 2009).

Regarding the critical effective viscosity value, we found $\eta_c \sim 10^{21}$ Pa s. Such a high viscosity corresponds in order of magnitudes to the one of hot sub-solidus host rocks inside which magma bodies are usually emplaced (Sparks et al., 2019). To our knowledge, for the specific case at APMB there are not many independent constraints on the viscosity of the lower-middle crust. A list of them is reported in Table 1. The viscosity of the partially molten zone has been inferred from resistivity maps by Comeau et al. (2016) who estimated a viscosity of $\eta \sim 10^{12} - 10^{16}$ Pa s with 20% melt fraction for the shallow magma reservoir. Viscosity of around $\eta \sim 10^{16} - 10^{18}$ Pa s has been estimated by Fialko and Pearse (2012) by assuming a linear Maxwell viscoelastic rheology for the lower-middle crust. Similar values ($< 10^{16}$ Pa s) are obtained by using the same viscoelastic rheology for the structure beneath APVC also by Gottsmann et al. (2017). However, although those values mainly represent either the viscosity of the APMB itself or that of the hot diapir rising from it, they do not give much information about the effective bulk viscosity of the whole inelastic crust. The latter should have in fact a reasonable larger value of η due to the contribution of the regions of the crust where both temperature and melt fraction are lower than the APMB's. Rheological measurements on larger timescales (i.e. millions of years) resulting from the analysis of lithosphere response to unloading of the

Table 1: Effective viscosities beneath APVC. "VE model" indicate simulations carried out with a viscoelastic (VE) rheology.

Technique	Viscosity (Pa s)	Reference
VE model	$\sim 10^{16} - 10^{18}$ for APMB	Fialko and Pearse (2012)
VE model	$< 10^{16}$ for APMB; $\sim 10^{16} - 10^{19}$ for diapir	Gottsmann et al. (2017)
VE model	$< 10^{21} - 10^{22}$ at ∼20 km beneath APVC	Gerbault et al. (2005)
from resistivity model	$< 10^{16}$ for APMB with 20% melt	Comeau et al. (2016)
from paleo-lake load	$<5\times10^{20}$ for crustal plate	Bills et al. (1994)

large paleo-lake in the Central Andes of Bills et al. (1994) give in fact a viscosity for the crustal plate that is larger than what predicted for APMB alone. The maximum effective bulk viscosity obtained in this way is η $<5\times10^{20}$ Pa s, definitely closer to the estimation for the maximum critical viscosity η_c we obtain by using a HB rheology (Fig. 8).

6. Conclusion

In this work we propose a mechanical interpretation for the well documented uplift above APMB, based on the assumption that the effective rheology at large scale of the crust is the one of a yield stress material. In material with such rheology, the diapir take-off and growth require two local conditions: (1) the ratio between yield stress and viscous stress to be supercritical ($Bi < 1$), and (2) the ratio between the buoyancy stress of the hot diapir and the yield stress to be larger than a critical value ($Y_{inv} > Y_{inv_C}$).

We find that in order to allow the formation and the rise of a 10-100 km-wide diapir from above APMB with a density contrast with respect to

surrounding rocks of 100-400 kg/m^3, the lower ductile crust needs a yield stress of $\sim$0.5-15 MPa to respect condition (1). Moreover, from condition (2) with an uplift velocity of 1 cm/yr, we can bound the maximum bulk effective viscosity η_c for the APMB lower-middle crust at $\eta_c \sim 10^{21}$ Pa s.

Appendix A. Details on experiments of thermal plumes

Figures 2 - 4 show the experiments on the development of thermal plumes in Carbopol of Davaille et al. (2013). These experiments are carried out by using a 166-mm-high rectangular tank into which the fluid is poured. The fluid is heated by a circular heater located at the center of the bottom surface. The maximal imposed temperature difference between the heater and the ambient fluid is $\Delta T \sim 44\,^{\circ}$C. The fluid rheology is described with a HB model with the following parameters: σ_y=0.10 Pa, n=0.54, K_v=0.76 Pa s^n. For the case in Figs. 2 - 4, the Rayleigh number at the onset of motion is

$$Ra = \frac{\alpha\,\rho\,g\,\Delta T h^3}{k\,\eta_c} \sim 10^6, \tag{A.1}$$

with α being the fluid thermal expansion (4.62×10^{-4} K^{-1}), ρ the density (1142 kg/m^3), k the thermal diffusivity (1×10^{-7} m^2/s), η_c the viscosity obtained from eq. (4) and h the height of the tank. The critical Yield number found in Davaille et al. (2013) ($Y_{inv_C} = 8.8 \pm 0.7$) can be determined from eq. (2) during stages (1) and (2) of plume development by assuming D=2 r_{eq}, with r_{eq} being the equivalent radius of a sphere having the same volume as the hot pocket. Experimentally, the hot pocket can be quantitatively defined within the temperature field by the isotherm $T_{lim} = 0.1\,\Delta T$, where

$\Delta T = T_{max} - T_{amb}$ and T_{max} is the heater temperature and T_{amb} the ambient temperature. The hot pocket is therefore represented by the volume of fluid with $T \geq T_{lim}$. For the density difference term in eq. (2) one can refer to the mean $\Delta\rho$ within the fluid pocket, that is $\Delta\rho \simeq \overline{\Delta\rho} = \alpha\rho(\overline{T}_{hot\,pocket} - T_{amb})$ where $\overline{T}_{hot\,pocket}$ is the average temperature of the pocket.

Acknowledgments

N.R. Sgreva was supported by the Initial Training Network No. 642029-ITN CREEP, an Horizon 2020 - Marie Sklodowska-Curie Action. This research was also supported by LabEx PALM (ANR-10-LABX-0039- PALM).

Data Availability

The data underlying this article will be shared on reasonable request to the corresponding author.

References

Ancey, C., 2007. Plasticity and geophysical flows: a review. Journal of Non-Newtonian Fluid Mechanics 142, 4–35.

Barnes, H.A., 1995. A review of the slip (wall depletion) of polymer solutions, emulsions and particle suspensions in viscometers: its cause, character, and cure. Journal of Non-Newtonian Fluid Mechanics 56, 221–251.

Beris, A., Tsamopoulos, J., Armstrong, R., Brown, R., 1985. Creeping motion of a sphere through a Bingham plastic. Journal of Fluid Mechanics 158, 219–244.

Bills, B.G., De Silva, S.L., Currey, D.R., Emenger, R.S., Lillquist, K.D., Donnellan, A., Worden, B., 1994. Hydro-isostatic deflection and tectonic tilting in the central Andes: Initial results of a gps survey of lake minchin shorelines. Geophysical Research Letters 21, 293–296.

Bonn, D., Denn, M.M., Berthier, L., Divoux, T., Manneville, S., 2017. Yield stress materials in soft condensed matter. Reviews of Modern Physics 89, 035005.

Burov, E.B., 2011. Rheology and strength of the lithosphere. Marine and Petroleum Geology 28, 1402–1443.

Caricchi, L., Burlini, L., Ulmer, P., Gerya, T., Vassalli, M., Papale, P., 2007. Non-newtonian rheology of crystal-bearing magmas and implications for magma ascent dynamics. Earth and Planetary Science Letters 264, 402–419.

Cashman, K.V., Sparks, R.S.J., Blundy, J.D., 2017. Vertically extensive and unstable magmatic systems: a unified view of igneous processes. Science 355, eaag3055.

Chmielowski, J., Zandt, G., Haberland, C., 1999. The central Andean Altiplano-Puna magma body. Geophysical Research Letters 26, 783–786.

Comeau, M.J., Unsworth, M.J., Cordell, D., 2016. New constraints on the magma distribution and composition beneath Volcán Uturuncu and the southern Bolivian Altiplano from magnetotelluric data. Geosphere 12, 1391–1421.

Comeau, M.J., Unsworth, M.J., Ticona, F., Sunagua, M., 2015. Magnetotelluric images of magma distribution beneath Volcán Uturuncu, Bolivia: Implications for magma dynamics. Geology 43, 243–246.

Coussot, P., 2005. Rheometry of pastes, suspensions, and granular materials: applications in industry and environment. John Wiley & Sons.

Coussot, P., Tocquer, L., Lanos, C., Ovarlez, G., 2009. Macroscopic vs. local rheology of yield stress fluids. Journal of Non-Newtonian Fluid Mechanics 158, 85–90.

Davaille, A., Gueslin, B., Massmeyer, A., Di Giuseppe, E., 2013. Thermal instabilities in a yield stress fluid: existence and morphology. Journal of Non-Newtonian Fluid Mechanics 193, 144–153.

Dinkgreve, M., Denn, M.M., Bonn, D., 2017. Everything flows?: Elastic effects on startup flows of yield-stress fluids. Rheologica Acta 56, 189–194.

Fialko, Y., Pearse, J., 2012. Sombrero uplift above the Altiplano-Puna magma body: Evidence of a ballooning mid-crustal diapir. Science 338, 250–252.

Gerbault, M., Martinod, J., Hérail, G., 2005. Possible orogeny-parallel lower crustal flow and thickening in the Central Andes. Tectonophysics 399, 59–72.

Gonnermann, H.M., Manga, M., 2007. The fluid mechanics inside a volcano. Annual Review of Fluid Mechanics 39, 321–356.

Gottsmann, J., Blundy, J., Henderson, S., Pritchard, M., Sparks, R., 2017. Thermomechanical modeling of the Altiplano-Puna deformation anomaly: Multiparameter insights into magma mush reorganization. Geosphere 13, 1042–1065.

Henderson, S., Pritchard, M., 2013. Decadal volcanic deformation in the Central Andes Volcanic Zone revealed by InSAR time series. Geochemistry, Geophysics, Geosystems 14, 1358–1374.

Jay, J.A., Pritchard, M.E., West, M.E., Christensen, D., Haney, M., Minaya, E., Sunagua, M., McNutt, S.R., Zabala, M., 2012. Shallow seismicity, triggered seismicity, and ambient noise tomography at the long-dormant Uturuncu Volcano, Bolivia. Bulletin of Volcanology 74, 817–837.

Jellinek, A.M., DePaolo, D.J., 2003. A model for the origin of large silicic magma chambers: precursors of caldera-forming eruptions. Bulletin of Volcanology 65, 363–381.

Jónsson, S., 2012. Tensile rock mass strength estimated using InSAR. Geophysical Research Letters 39.

Karimfazli, I., Frigaard, I., Wachs, A., 2016. Thermal plumes in viscoplastic fluids: Flow onset and development. Journal of Fluid Mechanics 787, 474–507.

Kreemer, C., Chamot-Rooke, N., 2004. Contemporary kinematics of the southern aegean and the mediterranean ridge. Geophysical Journal International 157, 1377–1392.

Kumar, R.R., Gordon, R.G., 2009. Horizontal thermal contraction of oceanic lithosphere: The ultimate limit to the rigid plate approximation. Journal of Geophysical Research: Solid Earth 114.

Makse, H.A., Brujic, J., Edwards, S.F., 2005. Statistical mechanics of jammed matter (2005). arXiv preprint cond-mat/0503081 .

Massmeyer, A., Di Giuseppe, E., Davaille, A., Rolf, T., Tackley, P.J., 2013. Numerical simulation of thermal plumes in a Herschel–Bulkley fluid. Journal of Non-Newtonian Fluid Mechanics 195, 32–45.

513 Massol, H., Jaupart, C., 2009. Dynamics of magma flow near the vent:
514 Implications for dome eruptions. Earth and Planetary Science Letters
515 279, 185 – 196.

516 Menand, T., Tait, S.R., 2001. A phenomenological model for precursor vol-
517 canic eruptions. Nature 411, 678–680.

518 Molnar, P., 2020. The brittle-plastic transition, earthquakes, temperatures,
519 and strain rates. Journal of Geophysical Research: Solid Earth 125,
520 e2019JB019335.

521 Pistone, M., Caricchi, L., Ulmer, P., Burlini, L., Ardia, P., Reusser, E.,
522 Marone, F., Arbaret, L., 2012. Deformation experiments of bubble-and
523 crystal-bearing magmas: Rheological and microstructural analysis. Jour-
524 nal of Geophysical Research: Solid Earth 117.

525 del Potro, R., Díez, M., Blundy, J., Camacho, A.G., Gottsmann, J., 2013. Di-
526 apiric ascent of silicic magma beneath the Bolivian Altiplano. Geophysical
527 Research Letters 40, 2044–2048.

528 Pritchard, M., De Silva, S., Michelfelder, G., Zandt, G., McNutt, S.R., Gotts-
529 mann, J., West, M., Blundy, J., Christensen, D., Finnegan, N., et al.,
530 2018. Synthesis: PLUTONS: Investigating the relationship between plu-
531 ton growth and volcanism in the Central Andes. Geosphere 14, 954–982.

532 Ranalli, G., 1995. Rheology of the Earth. Springer Science & Business Media.

533 Ranalli, G., 1997. Rheology and deep tectonics. Annals of Geophysics 40.

534 Rosenberg, C., Handy, M., 2005. Experimental deformation of partially
535 melted granite revisited: implications for the continental crust. Journal of
536 metamorphic Geology 23, 19–28.

537 Sgreva, N.R., 2020b. Influence of the fluid structure and elasticity on mo-
538 tions in a yield-stress material. Implications for geological systems. Theses.
539 Université Paris-Saclay. URL: http://www.theses.fr/2020UPASJ002.

540 Sgreva, N.R., Davaille, A., Kumagai, I., Kurita, K., 2020a. Interaction be-
541 tween a falling sphere and the structure of a non-newtonian yield-stress
542 fluid. Journal of Non-Newtonian Fluid Mechanics 284, 104355.

543 Spang, A., Baumann, T., Kaus, B.J., 2019. 3D geodynamic models of the
544 present-day Altiplano-Puna magmatic system. AGUFM 2019, V23H–0194.

545 Sparks, R., Annen, C., Blundy, J., Cashman, K., Rust, A., Jackson, M., 2019.
546 Formation and dynamics of magma reservoirs. Philosophical Transactions
547 of the Royal Society A 377, 20180019.

548 Tabuteau, H., Coussot, P., de Bruyn, J.R., 2007. Drag force on a sphere
549 in steady motion through a yield-stress fluid. Journal of Rheology 51,
550 125–137.

551 Turner, S., Costa, F., 2007. Measuring timescales of magmatic evolution.
552 Elements 3, 267–272.

553 Wang, H., Wright, T.J., Liu-Zeng, J., Peng, L., 2019. Strain rate distribution
554 in south-central Tibet from two decades of InSAR and GPS. Geophysical
555 Research Letters 46, 5170–5179.

Ward, K.M., Zandt, G., Beck, S.L., Christensen, D.H., McFarlin, H., 2014. Seismic imaging of the magmatic underpinnings beneath the Altiplano-Puna volcanic complex from the joint inversion of surface wave dispersion and receiver functions. Earth and Planetary Science Letters 404, 43–53.

Weinberg, R.F., Podladchikov, Y., 1994. Diapiric ascent of magmas through power law crust and mantle. Journal of Geophysical Research: Solid Earth 99, 9543–9559.

Zandt, G., Leidig, M., Chmielowski, J., Baumont, D., Yuan, X., 2003. Seismic detection and characterization of the Altiplano-Puna magma body, central Andes. Pure and Applied Geophysics 160, 789–807.